

Interpretable Geometry Sensitivity for Inverse Design of Integrated Photonics

Junho Park,^{1, a)} Taehan Kim,^{2, a)} Mohammad Ali,¹ and Di Liang¹

¹⁾*Department of Electrical and Computer Engineering, University of Michigan, Ann Arbor*

²⁾*College of Computing, Data Science, and Society, University of California, Berkeley*

(*Electronic mail: junhop@umich.edu)

(Dated: 3 March 2026)

As an increasingly powerful technique in integrated photonics, inverse design uses optimization algorithms to automatically create compact, high-performance photonic structures, often yielding non-intuitive layouts far more compact than conventional designs.^{1,2} While adjoint-based inverse design is a prominent optimization method, the resulting free-form layouts are difficult to interpret or diagnose under fabrication variability, even for experienced photonic device designers.³⁻⁵ We present an experimentally validated interpretability workflow that produces pixel-level sensitivity maps directly on the binary mask of an inverse-designed device. Using wavelength-division demultiplexers (WDMs) at 1310/1550 nm as examples, we train a lightweight convolutional surrogate to regress figures of merit (FoMs) and apply Integrated Gradients (IG) to attribute predicted transmission to individual pixels. We demonstrate that high-attribution hotspots correspond to physically meaningful substructures, such as splitter hubs and high-curvature edges. Experimental results show that controlled perturbations in these high-sensitivity regions result in up to an $\sim 11\times$ higher excess insertion loss compared to perturbations in non-sensitive regions, consistent with full-wave simulations. This approach adds a practical explainability layer to existing pipelines, offering a clear pathway for foundry-compatible design-rule checking and fabrication-aware constraint allocation without modifying the underlying electromagnetic solver.

I. INTRODUCTION

Adjoint-based inverse design has enabled compact nanophotonic devices for filtering, coupling, and routing by optimizing over high-dimensional design spaces (e.g., pixelated topology variables).²⁻⁴ In integrated photonics practice, however, the geometric complexity that enables performance can also hinder adoption: inverse-designed masks often contain small, non-intuitive features that are difficult to interpret, enforce with fabrication constraints, and debug when measured performance deviates from simulation.^{6,7} This lack of interpretability directly impacts design-rule checking, mask quality control, targeted Scanning Electron Microscopy (SEM) inspection, and principled simplification/cleanup for foundry integration.⁶

A core obstacle is that adjoint optimization provides gradients with respect to design variables,⁸ but does not directly yield a human-interpretable map of which *finalized* geometric features are most responsible for key metrics at specific operating wavelengths. Moreover, when a fabricated device underperforms, designers frequently resort to global re-optimization or ad-hoc edits, rather than localized, sensitivity-informed modifications.

In parallel, explainable artificial intelligence (XAI) methods such as Local Interpretable Model-agnostic Explanations (LIME)⁹ and Integrated Gradients (IG)¹⁰ have been developed to attribute model predictions to input features. These build upon earlier efforts in computer vision to produce saliency maps that visualize the internal representations of deep networks.¹¹ Among these methods,

IG is particularly attractive for photonic design layouts because it is gradient-based, preserves geometric structure, and can provide pixel-level attributions on the original input mask. These properties align naturally with binary photonic masks, motivating an interpretability layer that maps predicted optical metrics back to localized geometry.

Complementing these XAI frameworks, neural network based surrogate models serve as efficient estimators for the complex, high-dimensional mapping between photonic geometry and electromagnetic response.¹²⁻¹⁴ By providing a differentiable approximation of full-wave Maxwell solvers, these surrogates enable rapid exploration of design landscapes that are otherwise computationally intractable.

Our work suggests that a differentiable surrogate trained on diverse inverse-designed masks can be used as an “analysis instrument”: IG applied to the surrogate model yields a practical, mask-aligned sensitivity map that (i) highlights physically meaningful substructures (e.g., splitter hubs, tapers, sharp corners) and (ii) predicts which localized edits are likely to most affect transmission. We demonstrate the method on inverse-designed two-channel WDMs targeting O-band (1310 nm) and C-band (1550 nm), and we validate the pixel-level sensitivity map using matched-area region perturbations with FDTD simulation and experimental validation.

II. THEORY

Figure 1 illustrates the inverse-designed WDM geometry and modal operating context. We consider finalized inverse-designed two-channel WDMs with fixed input and output waveguides and a free-form design region represented

^{a)}These authors contributed equally to this work.

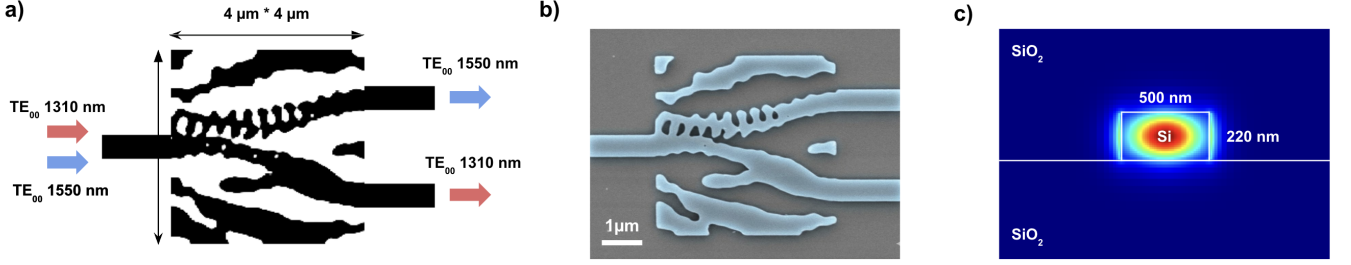


FIG. 1. (a) Inverse-designed two-channel WDM (1310/1550 nm) (b) SEM image of the fabricated WDM and (c) representative guided fundamental TE mode profile.

on a fabrication-aligned grid as a binary layout

$$\rho \in \{0, 1\}^{H \times W}, \quad (1)$$

with a minimum feature size of 100 nm.⁵ For various devices produced by the inverse-design pipeline, full-wave simulations provide spectral responses around 1310 nm and 1550 nm. FoMs are defined as transmitted power at these two target wavelengths.

In contrast to the inverse-design optimization stage, we treat the finalized mask ρ as a physical object and seek to determine which localized geometric features most strongly govern device performance. The objective is to quantify the sensitivity of transmission metrics to spatially localized perturbations of the layout and to validate these sensitivity predictions through controlled simulation and experimental measurements.

A. Data Generation of Various WDMs

We synthesize a corpus of inverse-designed WDM layouts using SPINS-B with fixed port geometry and randomized seeds and hyperparameters to induce layout diversity with different geometry and FoMs.^{4,15} Each inverse-design run outputs: (i) a finalized binary mask ρ and (ii) scalar FoMs. We use a dataset size of $N = 2200$. The key requirement is diversity in both geometry and spectral behavior so that the surrogate learns robust layout-to-FoM correlations rather than memorizing a narrow design family. The full interpretability pipeline with the surrogate is summarized in Fig. 2.

B. Convolutional Surrogate Model

We train a lightweight convolutional surrogate $F_\theta(\rho)$ to regress power at 1310 nm and 1550 nm from the binary layout. The training objective is mean-squared error (MSE):

$$\mathcal{L}(\theta) = \frac{1}{N} \sum_{n=1}^N \left(F_\theta(\rho^{(n)}) - y^{(n)} \right)^2, \quad (2)$$

where $y^{(n)}$ denotes the target FoM for the n -th mask.

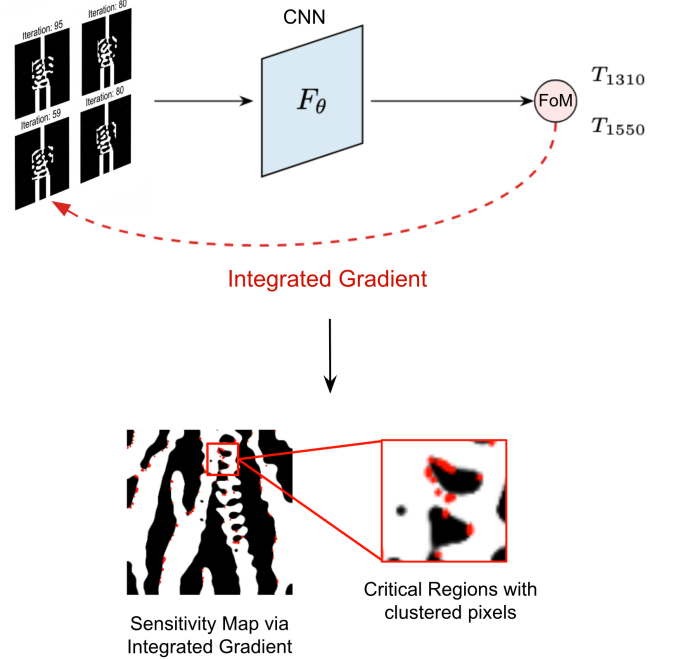


FIG. 2. Overview of the proposed interpretability workflow. A differentiable surrogate enables pixel-level attribution via Integrated Gradients, producing mask-aligned sensitivity maps and clustered critical regions for analysis and targeted edits.

We optimize using Adam (learning rate 10^{-3}), with early stopping (patience = 7) and model selection based on validation MSE. Indices are shuffled with a fixed random seed (42) and split into train/validation/test with a 70/15/15 ratio. The model converges within ~ 10 epochs and typical MSE values are on the order of 10^{-4} . We do not claim the surrogate replaces full-wave simulation; rather, it provides a differentiable mapping from mask to metric that enables gradient-based attribution. We validate the interpretability outputs by full-wave re-simulation under controlled perturbations and experimental agreement trends.

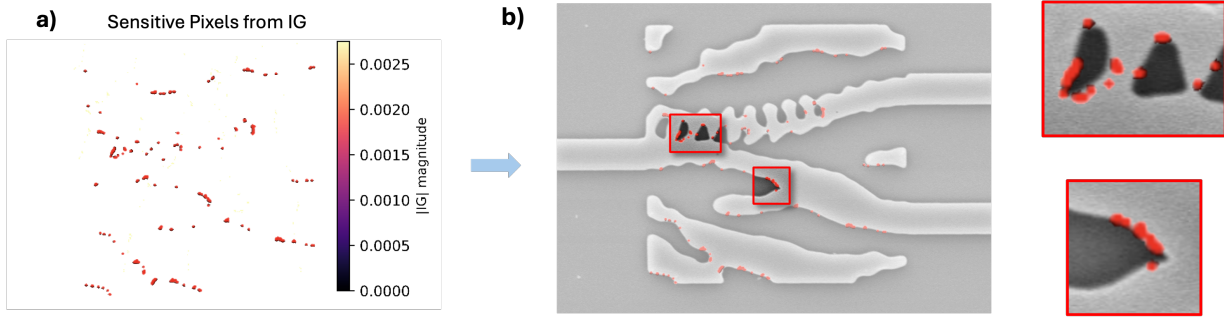


FIG. 3. IG sensitivity overlay and region selection. (a) Pixel-level IG attribution map (red = high magnitude). (b) Sensitivity map overlaid on SEM image of the unperturbed WDM. Colored boxes denote high-sensitivity regions with clustered pixels.

C. Pixel-Level Sensitivity Mapping via Integrated Gradients

To quantify how localized geometric features influence device performance, we compute a spatial sensitivity map directly on the binary layout mask ρ . We use IG applied to the differentiable surrogate $F_\theta(\rho)$ that predicts transmission metrics. For a given device, IG assigns a contribution value to each pixel,

$$IG_i = (\rho_i - \rho_{0,i}) \int_0^1 \frac{\partial F_\theta(\rho_0 + \alpha(\rho - \rho_0))}{\partial \rho_i} d\alpha, \quad (3)$$

which can be interpreted as the accumulated effect of that pixel on the predicted transmission as the layout transitions from a baseline geometry ρ_0 to the final design.

Because the mask encodes material distribution, IG_i serves as a proxy for how small, localized geometric perturbations affect modal coupling and interference, thereby providing a pixel-resolved map of performance sensitivity. IG can identify “high-sensitivity regions” by grouping clusters of pixels with the largest $|IG|$ values.

D. Perturbation Methodology: Matched-Area Region Edits

To validate the IG-derived sensitivity ranking with an apple-to-apple comparison, we generate perturbed masks using the same perturbation primitive and a matched edit budget across selected high-sensitivity regions. High-sensitivity Regions 1–3 are defined by clustered hotspot pixels (top-percentile of $|IG|$), while a non-sensitive control region is selected from near-zero attribution areas in the IG map (Fig. 3). We apply a “fill-in” perturbation that locally fills etched voids/small notches in the binary mask to emulate lithography/etch bias and corner rounding. For each region, the perturbation is constrained to the same perturbed area ($\sim 0.03 \mu\text{m}^2$; equivalently the same number of 100 nm-grid pixels), ensuring that observed degradation differences arise from *where* the edit is applied rather than perturbation magnitude or type. Fig. 4 show the perturbed area and the full SEM pictures of the perturbed masks. The same perturbed layouts are used for full-wave simulations and fabrication.

III. EXPERIMENT

A. Device Fabrication

Devices were fabricated on a standard silicon-on-insulator (SOI) platform with a 220 nm-thick silicon device layer on a $2 \mu\text{m}$ -thick buried oxide (BOX) layer. The inverse-designed free-form region contains subwavelength features approaching the 100 nm mask grid, requiring high-resolution lithography. Electron-beam lithography (EBL) was therefore used with proximity effect correction (PEC) to accurately define fine geometric details. A 300 nm ZEP520A resist layer was patterned in our in-house EBL with a high-resolution writing mode.

After resist development, an O_2 plasma descum was performed to remove residual resist, and the pattern was transferred into the full 220 nm silicon device layer using reactive ion etching (RIE). Remaining resist was stripped using Nanostrip at 60°C , and a $1 \mu\text{m}$ Plasma-enhanced Chemical Vapor Deposition SiO_2 overcladding was deposited at 350°C to complete the device stack.

Bias and exposure dose were calibrated to balance minimum achievable feature size with dimensional fidelity. Process optimization targeted faithful reproduction of the splitter/taper hub, high-curvature boundaries, and narrow features identified by the sensitivity analysis.

SEM inspection (Fig. 1b) confirms that the free-form region and port interfaces are faithfully transferred, including sub-100 nm features that often dominate sensitivity in inverse-designed layouts.

B. Optical Measurement

Optical characterization was performed using tunable laser sources covering the O-band and C-band, coupled to the chip via grating couplers. Polarization was adjusted to excite the fundamental TE mode. For each device, transmission into the intended output port was recorded over wavelength sweeps spanning the target bands.

Measured spectra were normalized to a reference waveguide on the same chip to remove coupling and

Perturbation on High Sensitivity Pixel Clusters

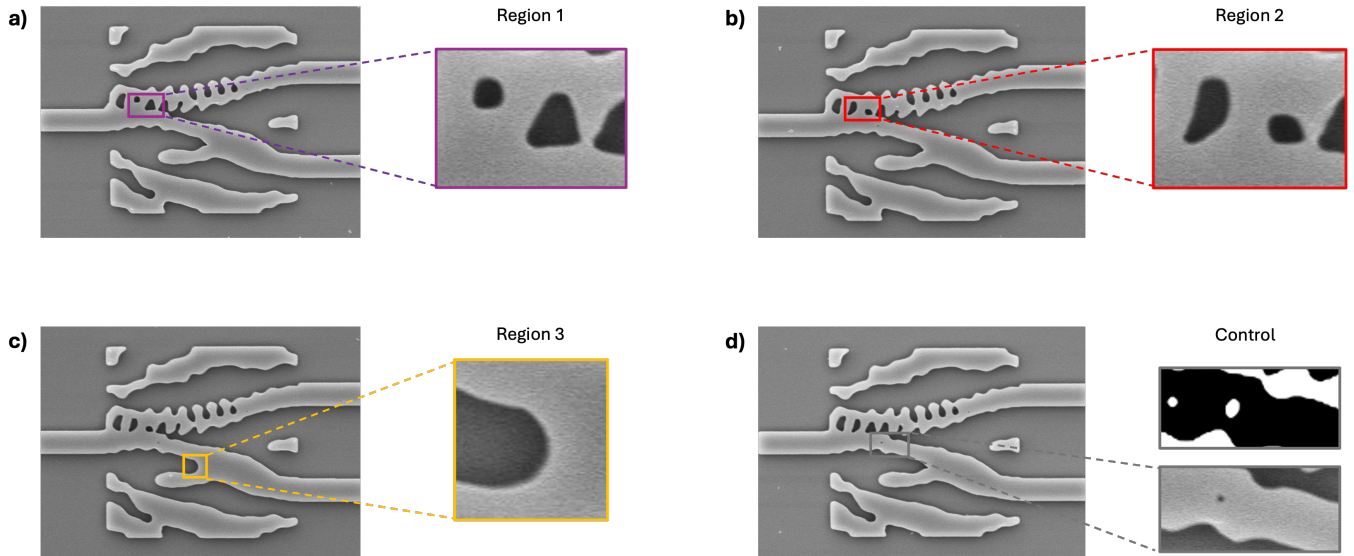


FIG. 4. SEM visualization of matched-area perturbations applied to IG-identified high-sensitivity regions and a low-sensitivity control. (a–c) SEM images of fabricated inverse-designed WDMs showing localized fill-in perturbations applied to three high-sensitivity regions (Regions 1–3) identified from clustered Integrated Gradients (IG) attribution hotspots. Insets show magnified views of the perturbed sub-regions. (d) SEM image of a low-sensitivity control region selected from IG-deprioritized areas, with corresponding mask-level perturbation and fabricated realization shown in the inset. All perturbations use the same geometric primitive and matched perturbed area ($\sim 0.03 \mu\text{m}^2$), ensuring that observed performance differences arise from *edit location* rather than perturbation magnitude or type.

propagation losses external to the device region; nevertheless, residual wavelength-dependent coupling mismatch and chip-scale inhomogeneity can introduce a small systematic offset relative to idealized simulations.

To isolate degradation induced by perturbations, we report excess insertion loss (EIL), defined relative to the unperturbed device in the same band:

$$\text{EIL}_{\text{device}} = \text{IL}_{\text{device}} - \text{IL}_{\text{Unperturbed}}. \quad (4)$$

This normalization suppresses common-mode offsets between experiment and simulation and directly quantifies the penalty attributable to localized edits.

IV. RESULTS

We first use IG to identify critical geometric substructures and define matched-area perturbation regions (Fig. 3). We then implement the corresponding localized “fill-in” edits in fabrication; Fig. 4 provides SEM verification of the matched-area perturbations for Regions 1–3 and the low-sensitivity control. Finally, we compare measured and simulated spectra and excess insertion loss to validate that IG-identified hotspots correspond to true fabrication-sensitive regions (Fig. 5 and Table I).

A. Sensitivity Maps

Pixel-level IG attribution produces spatially sparse sensitivity maps in which a limited subset of geometric features dominate device performance (Fig. 3). Hotspots consistently localize to high-curvature dielectric boundaries, abrupt width transitions, and the central splitter/taper hub responsible for modal conversion and phase partitioning. These regions align with known electromagnetic sensitivity mechanisms in silicon photonics¹⁶: curvature and corners enhance scattering loss, abrupt transitions introduce impedance discontinuities, and the hub controls modal superposition and relative phase that downstream geometry converts into wavelength-selective routing¹⁷.

This localization indicates that performance is governed by a small number of “structural control points,” while large portions of the free-form region exhibit near-zero attribution. Once the interference scaffold is established, many pixels become functionally redundant with respect to the evaluated FoMs, consistent with interference-based device physics.

B. FDTD Simulation

As mentioned above, matched-area fill-in perturbations were applied to both control and IG-identified high-sensitivity regions (SEM examples shown in Fig. 4), followed by full-wave FDTD re-simulation. Because perturbation type and area are fixed, degradation differences isolate the effect

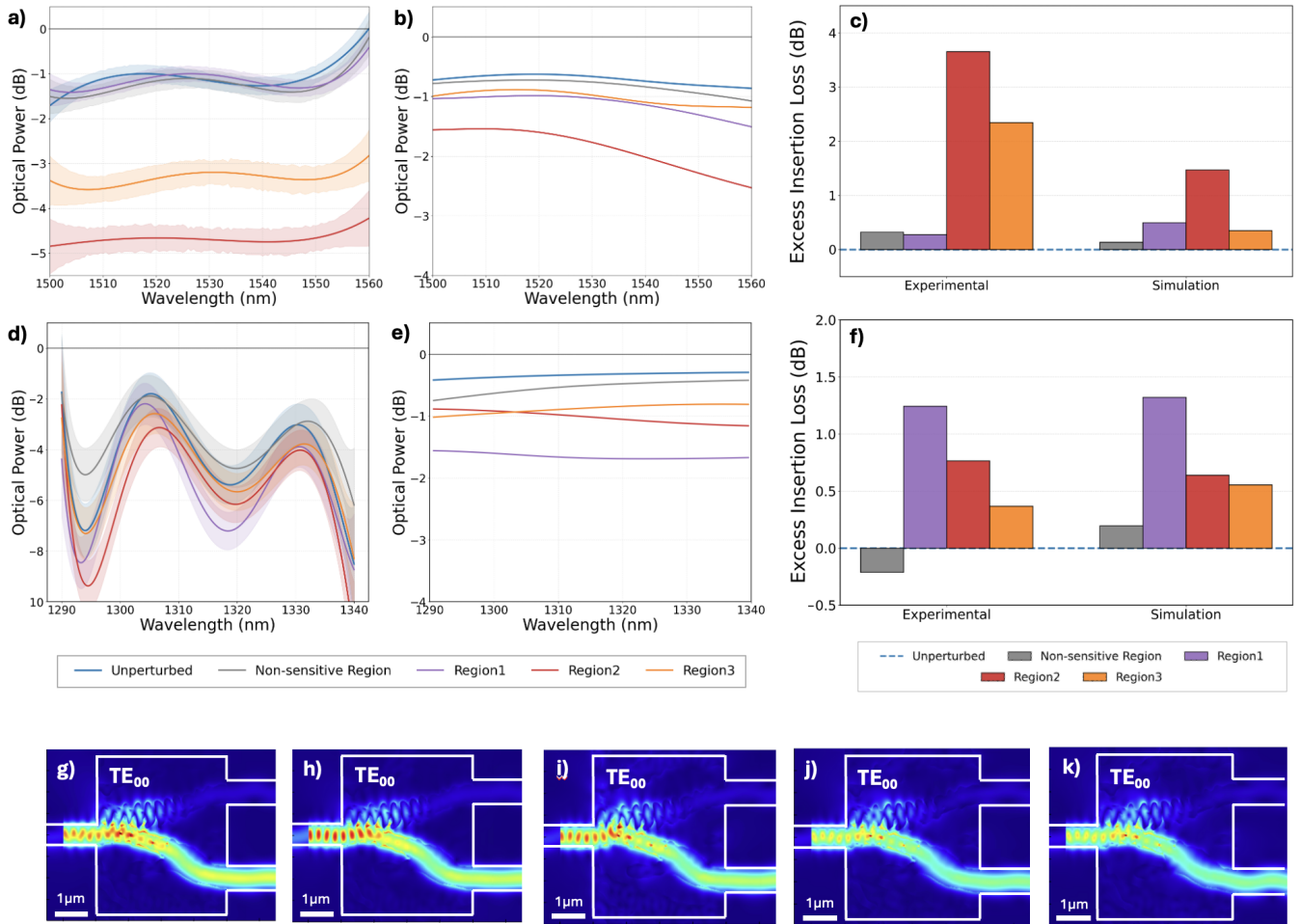


FIG. 5. Experimental and simulated validation of sensitivity-guided perturbations, with corresponding mode-propagation analysis. (a) Measured transmission spectra near 1550 nm (C-band) for the unperturbed device, low-sensitivity control, and high-sensitivity region edits. (b) Corresponding full-wave simulated transmission at 1550 nm. (c) Excess insertion loss (EIL) at 1550 nm comparing experiment and simulation, referenced to the unperturbed device. (d) Measured transmission spectra near 1310 nm (O-band). (e) Corresponding full-wave simulated transmission at 1310 nm. (f) EIL at 1310 nm for experiment and simulation. (g–k) Simulated electric-field intensity $|E|^2$ distributions of the fundamental TE_{00} mode at the O-band (1310 nm) for, in order, the unperturbed device, low-sensitivity control, and high-sensitivity perturbations applied to Regions 1, 2, and 3.

of *where* the geometry is modified.

Simulations show a clear quantitative separation (Fig. 5c and Fig. 5f, and Table I): high-sensitivity edits induce substantially larger EIL than control edits under identical perturbation budgets and produce positive EIL from the unperturbed baseline. At 1550 nm, simulated EIL increases from 0.134 dB (control) to 1.470 dB (Region 2), an $\sim 11\times$ increase. At 1310 nm, Region 1 produces 1.3215 dB EIL compared with 0.1960 dB for the control.

Mode-propagation analysis further clarifies the physical origin of this degradation (Fig. 5g–k). Perturbations in Regions 1 and 2 primarily reduce the transmitted $|E|^2$ magnitude at the output port while preserving the fundamental TE_{00} modal profile, consistent with increased scattering and phase imbalance. In contrast, the Region 3 perturbation (Fig. 5k) induces pronounced spatial oscillations near the output port, indicating unstable modal interference and

partial excitation of non-ideal field components. These observations confirm that attribution hotspots correspond to locations where small geometric changes strongly perturb modal interference and phase balance, ultimately degrading the device FoM.

C. Experimental Validation

Measured performance (Fig. 5 and Table I) preserves the simulation-predicted hierarchy. At 1550 nm, EIL rises from 0.320 dB (control) to 2.344 dB (Region 3) and 3.653 dB (Region 2), corresponding to an $\sim 11.4\times$ larger penalty for Region 2. At 1310 nm, Region 1 exhibits the largest EIL (1.2433 dB), followed by Region 2 (0.7636 dB) and Region 3 (0.3679 dB), while the control shows a small negative EIL consistent with normalization uncertainty.

TABLE I. Summary of experimental and simulated performance. For both 1550 nm and 1310 nm bands, insertion loss (IL) and excess insertion loss (EIL) are referenced to the unperturbed device in the same band. Exp denotes experimental and Sim denotes simulation.

Device	1550 nm (C-band)				1310 nm (O-band)			
	Exp IL	Exp EIL	Sim IL	Sim EIL	Exp IL	Exp EIL	Sim IL	Sim EIL
Unperturbed	0.595	0.000	0.812	0.000	2.9058	0.0000	0.3395	0.0000
Non-sensitive	0.915	0.320	0.946	0.134	2.6935	-0.2123	0.5354	0.1960
Region1	0.869	0.274	1.306	0.494	4.1491	1.2433	1.6609	1.3215
Region2	4.248	3.653	2.282	1.470	3.6694	0.7636	0.9781	0.6386
Region3	2.939	2.344	1.161	0.349	3.2737	0.3679	0.8939	0.5544

Simulation–experiment comparison. The experimental results preserve the simulation-predicted sensitivity hierarchy: regions identified as high-sensitivity in simulation consistently exhibit the largest excess insertion loss in fabricated devices, while control regions show minimal degradation. Experimental penalties, however, exceed simulated values at the most sensitive 1550 nm hotspots. This amplification is consistent with fabrication-induced scattering (sidewall and line-edge roughness, etch microloading) not captured in nominal-geometry FDTD, as well as nonlinear EBL/etch bias distortions that effectively increase perturbation severity in interference-critical regions. Grating-coupler reflections introduce additional Fabry–Pérot-like effects not included in simulation, further enhancing apparent loss¹⁸. At 1310 nm, Region 1 shows close agreement (1.2433 vs. 1.3215 dB), indicating degradation dominated by mode mismatch and phase error captured by the solver.

V. DISCUSSION

The spatial localization of hotspots aligns with established electromagnetic sensitivity mechanisms. High-curvature boundaries act as scattering centers, abrupt transitions introduce impedance discontinuities, and the splitter/taper hub controls modal phase partition. Perturbations in these regions disrupt interference balance, explaining the disproportionately large excess loss observed experimentally.

Free-form inverse-designed layouts lack the geometry-localized tolerance abstractions typical of PDK cells. The demonstrated sensitivity mapping translates complex masks into actionable manufacturing priorities. Hotspot-aware constraint allocation can enforce tighter feature rules only where performance is most sensitive, while sensitivity overlays guide metrology across the entire manufacturing flow, from mask reticle fabrication to wafer processing, to post-fabrication inspection, and ultimately failure analysis. Ranking geometry by functional importance supports reduced-order abstraction of free-form layouts, facilitating integration into PDK-style flows.

Sensitivity estimates derive from gradients of a learned surrogate rather than direct field-overlap sensitivities. Agreement between attribution trends, full-wave perturbation simulations, and measurements indicates that dominant

geometry–performance relationships are captured, though fabrication-induced scattering and measurement parasitics can amplify degradation beyond nominal simulations. Future work may incorporate fabrication-aware perturbations and uncertainty-aware surrogates to improve quantitative prediction.

VI. CONCLUSION

We demonstrated an experimentally validated framework for deriving pixel-level fabrication sensitivity maps from inverse-designed photonic layouts. The resulting attributions localize to electromagnetically critical substructures, and matched-area perturbation tests show that edits in these regions produce substantially larger excess insertion loss than geometrically equivalent edits in low-sensitivity areas. Agreement between simulation and fabricated-device measurements establishes that the learned sensitivity map corresponds to true interference- and fabrication-relevant device physics. Beyond interpretability, this approach provides a practical pathway toward tolerance-aware constraint allocation, targeted metrology, and manufacturability-informed abstraction of free-form inverse-designed components, supporting their integration into foundry-compatible photonic design workflows.

ACKNOWLEDGMENTS

The experimental portion of this work was performed in part at the University of Michigan Lurie Nanofabrication Facility. We also thank the Stanford NQP group for releasing SPINS-B used in this work.

DATA AVAILABILITY

The data that support the findings of this study are available from the corresponding author upon request.

¹J. S. Jensen and O. Sigmund, *Laser & Photonics Reviews* **5**, 308 (2011).

²S. Molesky, Z. Lin, A. Y. Piggott, W. Jin, J. Vucković, and A. W. Rodriguez, *Nature Photonics* **12**, 659 (2018).

³C. M. Lalau-Keraly, S. Bhargava, O. D. Miller, and E. Yablonovitch, *Optics express* **21**, 21693 (2013).

- ⁴L. Su, D. Vercruyse, J. Skarda, N. V. Sapro, J. A. Petykiewicz, and J. Vuckovic, "Nanophotonic inverse design with spins: Software architecture and practical considerations," (2019), arXiv:1910.04829 [physics.app-ph].
- ⁵A. Y. Piggott, J. Lu, K. G. Lagoudakis, J. Petykiewicz, T. M. Babinec, and J. Vučković, *Nature photonics* **9**, 374 (2015).
- ⁶A. M. Hammond, A. Oskooi, S. G. Johnson, and S. E. Ralph, *Optics Express* **29**, 23916 (2021).
- ⁷A. Y. Piggott, J. Petykiewicz, L. Su, and J. Vučković, *Scientific reports* **7**, 1786 (2017).
- ⁸O. D. Miller, *Photonic design: From fundamental solar cell physics to computational inverse design* (University of California, Berkeley, 2012).
- ⁹M. T. Ribeiro, S. Singh, and C. Guestrin, in *Proceedings of the 22nd ACM SIGKDD international conference on knowledge discovery and data mining* (2016) pp. 1135–1144.
- ¹⁰M. Sundararajan, A. Taly, and Q. Yan, in *International conference on machine learning* (PMLR, 2017) pp. 3319–3328.
- ¹¹K. Simonyan, A. Vedaldi, and A. Zisserman, arXiv preprint arXiv:1312.6034 (2013).
- ¹²J. Peurifoy, Y. Shen, L. Jing, Y. Yang, F. Cano-Renteria, B. G. DeLacy, J. D. Joannopoulos, M. Tegmark, and M. Soljačić, *Science advances* **4**, eaar4206 (2018).
- ¹³P. R. Wiecha, A. Arbouet, C. Girard, and O. L. Muskens, *Photonics Research* **9**, B182 (2021).
- ¹⁴D. Liu, Y. Tan, E. Khoram, and Z. Yu, *Acs Photonics* **5**, 1365 (2018).
- ¹⁵"Spins-b documentation," <https://spins-b.readthedocs.io/en/latest/>, accessed 2026-02-02.
- ¹⁶F. Wang, J. S. Jensen, and O. Sigmund, *Journal of the Optical Society of America B* **28**, 387 (2011).
- ¹⁷F. P. Payne and J. P. Lacey, *Optical and Quantum Electronics* **26**, 977 (1994).
- ¹⁸Y. Wang, X. Wang, J. Flueckiger, H. Yun, W. Shi, R. Bojko, N. A. Jaeger, and L. Chrostowski, *Optics express* **22**, 20652 (2014).